

# Competing Photocurrent Mechanisms in Quasi-Metallic Carbon Nanotube *pn* Devices

Moh. R. Amer, Shun-Wen Chang, and Stephen B. Cronin\*

In recent years, the optoelectronic properties of graphene and carbon nanotube devices have been investigated by several research groups.<sup>[1–7]</sup> Graphene field-effect-transistors with a double gate structure exhibit a photocurrent originating from a photothermoelectric effect in which the optical excitation creates a temperature gradient.<sup>[8]</sup> The thermoelectric diffusion of carriers from the hot region to the cold region results in the measured photovoltage/photocurrent. Extensive studies on semiconducting carbon nanotube devices have been carried out, reporting multiple electron-hole pair generation,<sup>[9]</sup> ideal diode behavior,<sup>[10]</sup> photovoltaic effect,<sup>[11]</sup> and photothermoelectric effect.<sup>[12,13]</sup> Barkelid and Zwiller investigated the photothermoelectric effect in quasi-metallic carbon nanotube split gates,<sup>[14]</sup> where their photocurrent is a strong function of the nanotube's thermoelectric power. Moreover, quasi-metallic carbon nanotube *pn* devices have shown rectifying behavior and Zener breakdown under reverse bias.<sup>[15]</sup> This rectifying behavior occurs due to anomalously large bandgaps, which exceed theoretically predicted bandgaps by 200%–400%.<sup>[16–19]</sup> These large quasi-metallic bandgaps are only observed in ultraclean nanotubes suspended off the substrate.<sup>[16,20]</sup> Otherwise, inhomogeneities induced by the underlying substrate smear the band edges, making the bandgaps appear smaller. The bandgap in nominally “metallic” nanotubes (i.e.,  $(n-m)\bmod 3 = 0$ ) arises from the curvature of the nanotube, which mixes the  $\pi$  and  $\sigma$  orbitals and opens a

bandgap.<sup>[17]</sup> These previous calculations, however, are based on local density approximation (LDA) methods, which are known to underestimate bandgap values substantially. These bandgap values, ranging from 0 to 180 meV, are smaller than those of any known bulk material and fall in the terahertz and far infrared regime. Such carbon nanotube materials are potential candidates for realizing Terahertz and far infrared optoelectronic devices.<sup>[21–24]</sup>

In the work presented here, we systematically investigate the mechanisms underlying photocurrent generation in quasi-metallic nanotubes over a wide range of bandgaps (30–180 meV). Here, *pn*-junctions are formed by electrostatic doping using two gate electrodes positioned beneath individual suspended nanotubes. We measure the photocurrent as a function of the electrostatic doping. We correlate homogenous *pn*-doping dependence ( $V_{g1} = -V_{g2}$ ) of the photocurrent with the current–voltage ( $I$ – $V_g$ ) characteristics ( $V_{g1} = V_{g2}$ ) of each device. These  $I$ – $V_g$  characteristics, in turn, are used to determine the bandgap of the nanotubes by fitting our data to a Landauer transport model. The mechanism underlying photocurrent generation is then established by correlating the photocurrent transport with the calculated thermoelectric power, the measured conductance, and the extracted bandgap for all devices.

**Figure 1a** shows a schematic diagram along with a SEM image of the device under investigation. The lithography and fabrication steps as well as the experimental setup are discussed in the Experimental Section. **Figure 2a,b** shows photocurrent maps of two different 4- $\mu\text{m}$  long suspended CNT devices plotted as a function of all possible gate-doping conditions. We observe two distinct trends in this data. In the first trend, shown in **Figure 2a**, the photocurrent magnitude reaches a maximum at low *pn/np* concentrations (e.g.,  $V_{g1} = 2$  and  $V_{g2} = -1$ ) and then decreases with increasing electrostatic doping (e.g.,  $V_{g1} = 6$  and  $V_{g2} = -6$ ). In this **Figure**, we notice the sixfold pattern, which is characteristic of the photothermoelectric effect.<sup>[8]</sup> In **Figure 2b**, however, a different trend is observed, where the photocurrent reaches a maximum value and then saturates with increasing electrostatic *pn/np* doping, which we attribute to photovoltaic charge separation, where a built-in electric field separates the electron-hole pair causing photocurrent to flow in the nanotube.

**Figure 3** shows the photocurrent versus *pn*-doping profiles for four different nanotube devices under equal and opposite gate potentials (i.e.,  $V_{g1} = -V_{g2}$ ). The conductance curves of these devices are also plotted in the insets of these figures. Here, two distinct trends can be seen in **Figure 3a–d**. For

M. R. Amer  
Center of Excellence for Green Nanotechnologies  
University of California  
Los Angeles, CA 90095  
USA and King Abdulaziz City for Science  
and Technology  
Riyadh, Saudi Arabia  
S.-W. Chang, S. B. Cronin  
Department of Physics and Astronomy  
University of Southern California  
Los Angeles, CA 90089, USA  
E-mail: scronin@usc.edu  
S. B. Cronin  
Department of Electrical Engineering  
University of Southern California  
Los Angeles, CA 90089, USA  
S. B. Cronin  
Department of Material Science  
University of Southern California  
Los Angeles, CA 90089, USA  
DOI: 10.1002/sml.201403413



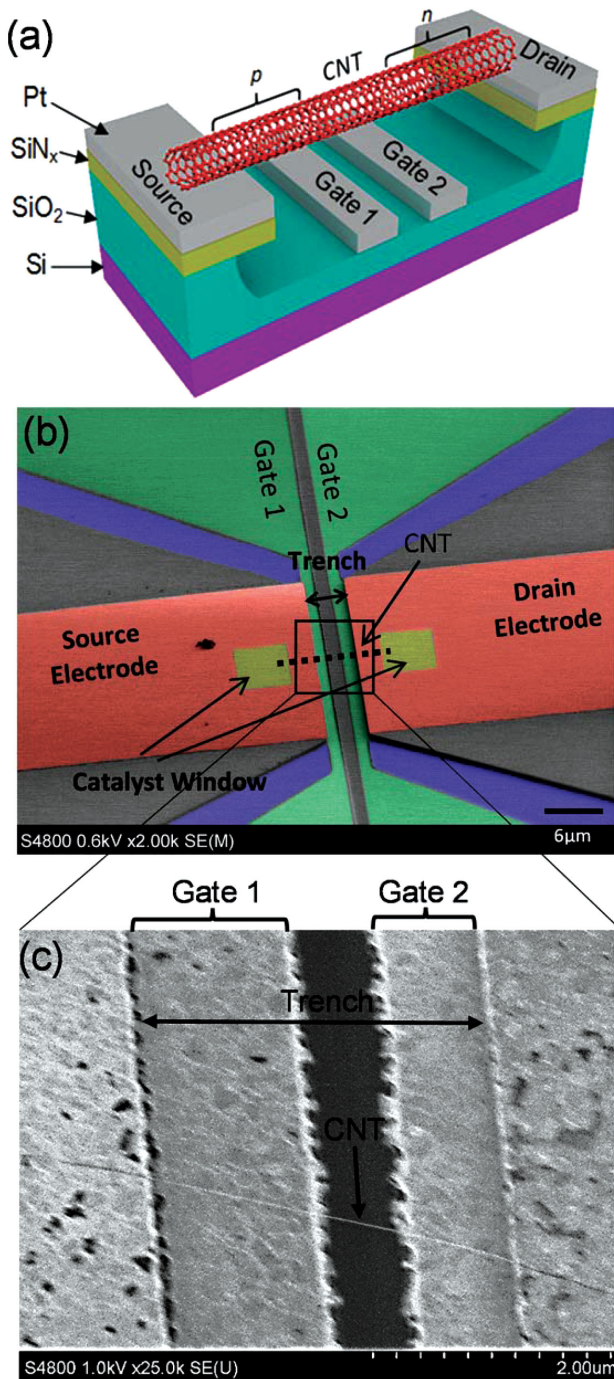


**Figure 1.** Split gate quasi-metallic nanotube geometry. a) Schematic diagram and b,c) SEM images of the final *pn*-device structure.

Devices 1 and 3, the photocurrent profile shows a nonmonotonic function with equal and opposite *pn* doping, while the  $I-V_g$  curves of these devices exhibit a slight dip in the conductance at the charge neutrality point, indicating that these quasi-metallic nanotubes have relatively small bandgaps. This nonmonotonic profile is consistent at different laser powers, as illustrated in Figure S3 (Supporting Information). For Devices 2 and 4, the photocurrent profile shows a monotonic profile that saturates at a constant value with increasing *pn* doping. These devices exhibit a large dip in the conductance-gate voltage

curves at the charge neutrality point, where the conductance is modulated by at least 73%. We attribute the former profiles (Figures 3a,c) to photothermoelectric effect and the latter profiles (Figures 3b,d) to photovoltaic effect, as explained below. These two different types of behaviors indicate that quasi-metallic nanotubes can exhibit photothermoelectric and photovoltaic effects, depending on the magnitude of the bandgap.

The measured photocurrent of Devices 1 and 3 can be modeled by calculating the thermoelectric power (i.e., Seebeck coefficient) of the nanotube. The photothermoelectric photocurrent is proportional to the thermoelectric power, and can be calculated based on the  $I-V_g$  characteristics measured for these devices according to the following expression<sup>[25]</sup>

$$I_{\text{ph}} = \frac{(S_2 - S_1)\Delta T}{R} \quad (1)$$

where  $S$  is the thermoelectric power,  $\Delta T$  is the temperature difference between the center and ends of the nanotube, and  $R$  is the resistance of the device. The thermoelectric power is given by the Mott formula according to<sup>[13]</sup>

$$S = \frac{-\pi^2 k_B T}{3e} \frac{1}{G} \frac{dG}{dV_g} \frac{dV_g}{dE} \quad (2)$$

where  $k_B$  is the Boltzmann constant,  $T$  is the temperature, and  $G$  is the nanotube conductance. The term,  $\frac{dG}{dV_g}$  is taken from the measured conductance versus gate-voltage curve (shown in the insets of Figure 3). The relation between the gate voltage and the Fermi energy is established from fits of our conductance-gate voltage data using a Landauer transport model<sup>[16,26–28]</sup> given by

$$G_{\text{CNT}} = \frac{1}{R_{\text{CNT}}} = \left( \frac{4e^2}{h} \right) \int_{-\infty}^{\infty} \left( \frac{\lambda_{\text{eff}}(E, T)}{\lambda_{\text{eff}}(E, T) + L} \right) \left( \frac{\partial f}{\partial E} \right) dE \quad (3)$$

Here,  $\lambda_{\text{eff}}$  is the effective mean free path for electrons in the system given by Mathiessen's rule.<sup>[16,26,29]</sup> The integral is taken over the density of states ( $D$ ), which is given by

$$D(E) = \sum_{j=1}^N \left| \frac{dE_j(k)}{dk} \right|^{-1} \quad (4)$$

where the derivative is taken over a hyperbolic dispersion relation with a small bandgap. Figure S5 (Supporting Information) shows the Landauer model fits to the measured conductance curves for all samples measured in this study. Accordingly, in **Figure 4a**, the thermoelectric power calculated in this fashion is plotted for Device 3 in Figure 3c. The excellent agreement between the measured photocurrent profile (Figure 3a) and the calculated thermoelectric power (Figure 4a) indicates that the photocurrent generation is photothermoelectric in origin.

The photocurrent in Devices 2 and 4, shown in Figure 3b,d, reaches a maximum and stays constant over a wide range of *pn*/*np* doping. The extracted thermoelectric power for Device 4 is plotted in Figure 4b. As illustrated, this model fails to

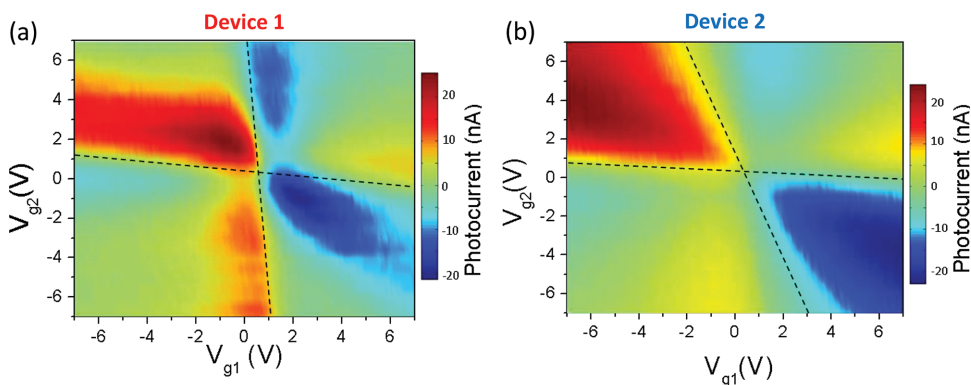


**Figure 2.** Photocurrent measurements on quasi-metallic nanotube devices. Generated photocurrent maps measured for all different combinations of gate voltage 1 and 2 of a) Device 1, and b) Device 2.

produce the observed photocurrent profile in Figure 3d. A more appropriate model that fits the photocurrent profile for this class of devices is the photovoltaic effect, where the built-in potential of the *pn*-junctions is strong enough to break the exciton binding energy (Figure S4, Supporting Information). For quasi-metallic nanotubes, recent experiments show that the exciton binding energy from the optical absorption spectra is on the order of 50 meV.<sup>[30]</sup> In photovoltaic devices, the maximum built-in voltage (and hence built-in electric field) attained inside the junction is set by the bandgap of the material. In our case, these quasi-metallic

nanotubes exhibit anomalously large bandgaps, larger than 50 meV. The expected built-in voltage is in the same order as the bandgap of these nanotubes, which is comparable with the exciton binding energy. Accordingly, we deduce that quasi-metallic nanotubes with bandgap magnitudes larger than the exciton binding energy are capable of showing the photovoltaic effect.

In **Figure 5**, we compare the electron transport measurements for devices that exhibit identical device length, but showed different photocurrent profiles. As expected, due to the existence of the anomalously large bandgap in devices

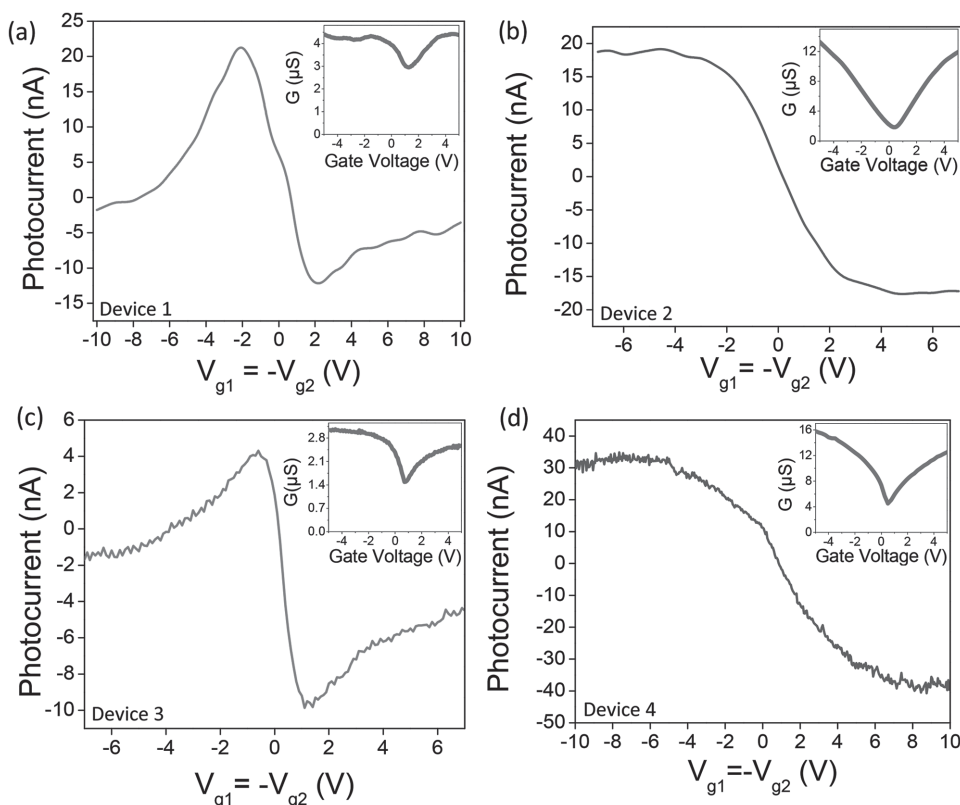


**Figure 3.** Measured photocurrent of homogeneous *pn* doping. Measured photocurrent plotted as a function of electrostatic *pn* doping ( $V_{g1} = -V_{g2}$ ) of four different devices. The measured photocurrent shows a nonmonotonic profile for a) Device 1 and c) Device 3. For b) Device 2 and d) Device 4, however, the measured photocurrent saturates with increasing electrostatic doping. The insets show the measured conductance versus gate voltage of each device, taken with  $V_{g1} = V_{g2}$ .

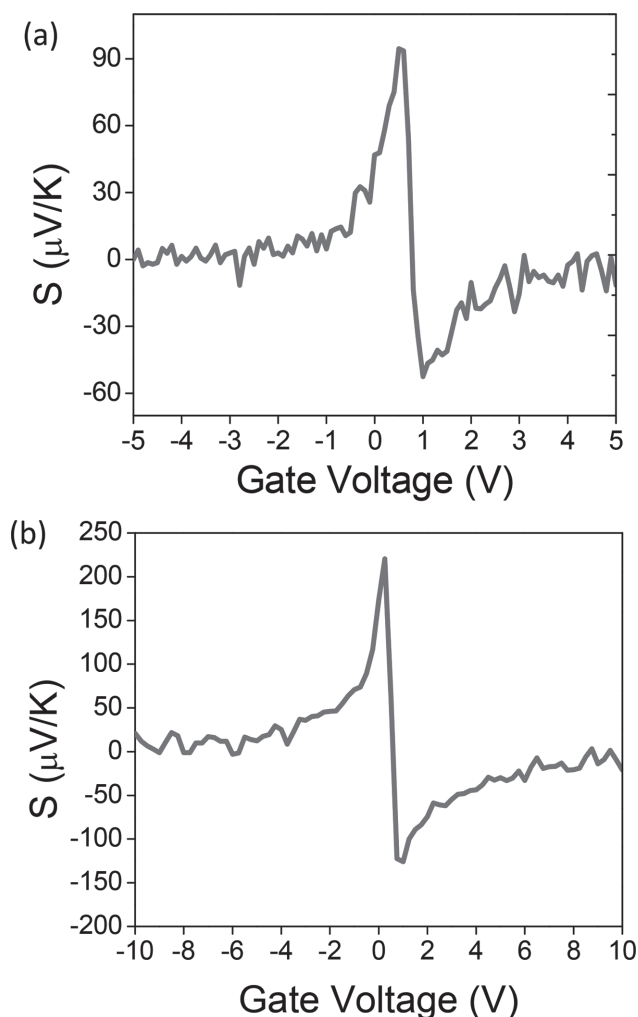


**Figure 4.** Thermoelectric power. The calculated thermoelectric power of a) Device 3 in Figure 2c and b) Device 4 in Figure 2d. For Device 3, the thermoelectric power profile is in excellent agreement with the measured photocurrent profile. While for Device 4, the measured photocurrent profile does not follow the calculated thermoelectric power profile,

with photovoltaic effect, the conductance modulation of Device 2 and 4 is large, reaching 90% and 73%, respectively,

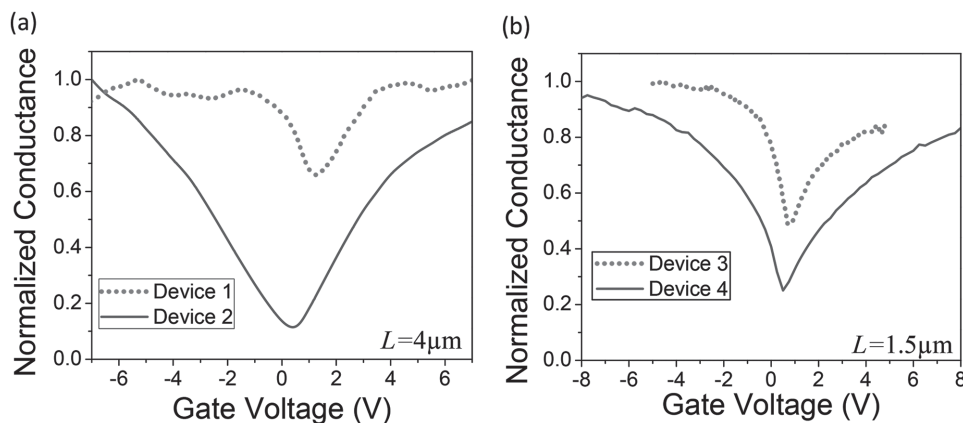


**Figure 5.** Conductance comparison and bandgap modulation. The normalized conductance of a) Device 1 (dotted red curve) and Device 2 (blue solid curve). Both of these devices are  $\approx 4\text{-}\mu\text{m}$  long. b) Device 3 (dotted red curve) and Device 4 (blue solid curve). Both of these devices are  $\approx 1.5\text{-}\mu\text{m}$  long.

compared with Device 1 and Device 3, which only varies by 30% and 50%, respectively. **Table 1** shows a summary of the results obtained on a total of five different devices, which lists the bandgap, change in conductance ( $\Delta G/G_{\text{max}}$ ), the photocurrent profile observed, and the associated photocurrent mechanism. We find that devices with bandgaps below 50 meV exhibit photocurrent due to the photothermoelectric effects (i.e., nonmonotonic photocurrent gate dependence). Whereas, devices with bandgaps above 80 meV (anomalously large) exhibit photocurrent saturation with increasing  $pn$ -doping concentrations indicative of photovoltaic behavior. This sets a lower limit for the bandgap above, which the photovoltaic effect becomes the dominant mechanism for photocurrent generation in  $pn$ -doped carbon nanotubes.

In conclusion, quasi-metallic nanotube  $pn$  devices show two different trends in their photocurrent behavior. For devices with a small dip in the conductance ( $E_{\text{gap}} \leq 50$  meV), the photocurrent is a nonmonotonic function of electrostatic  $pn$  doping (i.e.,  $V_{g1} = -V_{g2}$ ), and the measured photocurrent profile agrees with the photothermoelectric model. For devices that exhibit bandgaps larger than  $E_{\text{gap}} \geq 80$  meV, the photocurrent saturates to a constant value over a wide range of  $pn/np$ -doping conditions. The fundamental photocurrent effect for these devices is photovoltaic in origin, where the built-in voltage magnitude is sufficiently large to break the exciton binding energy. These optoelectronic measurements shed light on the unique photophysics associated with anomalously large bandgaps in quasi-metallic carbon nanotubes.

## Experimental Section

**Fabrication:** Devices are fabricated by first etching a 500-nm deep, 4- $\mu\text{m}$  wide trench in pregrown silicon nitride (100-nm thick) on silicon oxide (1- $\mu\text{m}$  thick) on silicon, as illustrated in Figure 1a. Pt electrodes are deposited on top of the silicon nitride, which act as the source and drain electrodes, and two 1- $\mu\text{m}$  wide gate electrodes are deposited in the trench with 1  $\mu\text{m}$  separation. Iron catalyst is deposited on top of the source and drain electrodes for nanotube growth, which occurs at 875  $^{\circ}\text{C}$  for 10 min, using ethanol as the carbon feedstock.<sup>[16,31–33]</sup> As the nanotube growth is the

**Table 1.** The extracted bandgap, conductivity modulation, and the photocurrent mechanism observed in five different devices. In the last column, photovoltaic effect and photothermoelectric effect are abbreviated as (PV) and (PTE), respectively.

Device	Bandgap [meV]	$[\Delta G/G_{\max}]$	Photocurrent profile observed	Photocurrent mechanism
Device 1	30	30%	Nonmonotonic	PTE
Device 2	170	90%	Monotonic	PV
Device 3	48	50%	Nonmonotonic	PTE
Device 4	81	73%	Monotonic	PV
Device 5	180	97%	Monotonic	PV

last step in the sample fabrication process, this method ensures that the nanotube is not contaminated by any chemical residues from the lithographic processes.

**Characterization:** Devices are considered by measuring the  $I-V_{\text{bias}}$  characteristics under high bias for each device. Devices that show a maximum current  $I_{\text{max}} \approx 10/L$ , where  $L$  is the trench width in micrometer and  $I_{\text{max}}$  is in microampere, correspond to individual carbon nanotubes and are selected for further study.<sup>[26,31,33,34]</sup> Raman spectra of these individual quasi-metallic nanotubes along with photocurrent spectra are measured as shown in the (Figures S1,S2, Supporting Information).

**Photocurrent Experimental Setup:** For all Devices, an optical cryostat stage is mounted under a microscope for electrical biasing. A 633-nm laser is focused through an objective lens on the middle portion of the nanotube, where the *pn*-junction is located. Before laser illumination, the Device is gated in a *pn*/*np* configuration. We used 2.9 kW cm<sup>-2</sup> laser power. Photocurrent is measured at the source electrode with the drain electrode being grounded. A lock-in technique is used to measure low photocurrent values.

## Supporting Information

Supporting Information is available from the Wiley Online Library or from the author.

## Acknowledgements

This work was supported in part by Department of Energy (DOE) Award No. DE-FG02-07ER46376. A portion of this work was carried out in the University of California Santa Barbara (UCSB) nanofabrication facility, part of the NSF funded National Nanotechnology Infrastructure Network (NNIN) network. We would like to acknowledge KACST for their support through the Center of Excellence for Green Nanotechnologies (CEGN) at UCLA and KACST.

- [1] M. Freitag, Y. Martin, J. Misewich, R. Martel, P. Avouris, *Nano Lett.* **2003**, *3*, 1067.  
 [2] D. Mann, Y. Kato, A. Kinkhabwala, E. Pop, J. Cao, X. Wang, L. Zhang, Q. Wang, J. Guo, H. Dai, *Nature Nanotechnol.* **2007**, *2*, 33.

- [3] T. Mueller, M. Kinoshita, M. Steiner, V. Perebeinos, A. A. Bol, D. B. Farmer, P. Avouris, *Nature Nanotechnol.* **2009**, *5*, 27.  
 [4] M. Steiner, M. Freitag, V. Perebeinos, A. Naumov, J. P. Small, A. A. Bol, P. Avouris, *Nano Lett.* **2009**, *9*, 3477.  
 [5] D. Stewart, F. Léonard, *Phys. Rev. Lett.* **2004**, *93*, 107401.  
 [6] F. Bonaccorso, Z. Sun, T. Hasan, A. Ferrari, *Nature Photon.* **2010**, *4*, 611.  
 [7] A. Pospischil, M. Humer, M. M. Furchi, D. Bachmann, R. Guider, T. Fromherz, T. Mueller, *Nature Photon.* **2013**, *7*, 892.  
 [8] N. M. Gabor, J. C. Song, Q. Ma, N. L. Nair, T. Taychatanapat, K. Watanabe, T. Taniguchi, L. S. Levitov, P. Jarillo-Herrero, *Science* **2011**, *334*, 648.  
 [9] N. M. Gabor, Z. Zhong, K. Bosnick, J. Park, P. L. McEuen, *Science* **2009**, *325*, 1367.  
 [10] J. U. Lee, P. Gipp, C. Heller, *Appl. Phys. Lett.* **2004**, *85*, 145.  
 [11] J. U. Lee, P. J. Codella, M. Pietrzykowski, *Appl. Phys. Lett.* **2007**, *90*, 053103.  
 [12] L. Aspirtarte, T. DeBorde, T. Sharf, J. Kevek, E. Minot, *Bull. Am. Phys. Soc.* **2014**, *59*, 216.  
 [13] J. P. Small, K. M. Perez, P. Kim, *Phys. Rev. Lett.* **2003**, *91*, 256801.  
 [14] M. Barkelid, V. Zwiller, *Nature Photon.* **2014**, *8*, 47.  
 [15] M. R. Amer, S.-W. Chang, R. Dhall, J. Qiu, S. B. Cronin, *Nano Lett.* **2013**, *13*, 5129.  
 [16] M. R. Amer, A. Bushmaker, S. B. Cronin, *Nano Lett.* **2012**, *12*, 4843.  
 [17] C. L. Kane, E. Mele, *Phys. Rev. Lett.* **1997**, *78*, 1932.  
 [18] M. Ouyang, J.-L. Huang, C. L. Cheung, C. M. Lieber, *Science* **2001**, *292*, 702.  
 [19] A. Kleiner, S. Eggert, *Phys. Rev. B* **2001**, *63*, 073408.  
 [20] V. V. Deshpande, B. Chandra, R. Caldwell, D. S. Novikov, J. Hone, M. Bockrath, *Science* **2009**, *323*, 106.  
 [21] A. Ugawa, A. G. Rinzler, D. Tanner, *Phys. Rev. B* **1999**, *60*, R11305.  
 [22] X. He, N. Fujimura, J. M. Lloyd, K. J. Erickson, Q. Zhang, W. Gao, Q. Jiang, Y. Kawano, R. H. Hauge, F. Leonard, J. Kono, *Nano Lett.* **2014**, *14*, 3953.  
 [23] T. Kampfrath, K. von Volkman, C. Aguirre, P. Desjardins, R. Martel, M. Krenz, C. Frischkorn, M. Wolf, L. Perfetti, *Phys. Rev. Lett.* **2008**, *101*, 267403.  
 [24] M. Portnoi, O. Kibis, M. Rosenau da Costa, *Superlattices Microstruct.* **2008**, *43*, 399.  
 [25] X. Xu, N. M. Gabor, J. S. Alden, A. M. van der Zande, P. L. McEuen, *Nano Lett.* **2009**, *10*, 562.  
 [26] A. W. Bushmaker, V. V. Deshpande, S. Hsieh, M. W. Bockrath, S. B. Cronin, *Nano Lett.* **2009**, *9*, 2862.  
 [27] S. Datta, *Electronic Transport in Mesoscopic Systems*, Cambridge University Press, Cambridge, **1997**.  
 [28] Y. Zhao, A. Liao, E. Pop, *IEEE Electron Device Lett.* **2009**, *30*, 1078.  
 [29] S.-W. Chang, R. Dhall, M. Amer, K. Sato, R. Saito, S. Cronin, *Nano Res.* **2013**, *6*, 736.  
 [30] F. Wang, D. J. Cho, B. Kessler, J. Deslippe, P. J. Schuck, S. G. Louie, A. Zettl, T. F. Heinz, Y. R. Shen, *Phys. Rev. Lett.* **2007**, *99*, 227401.  
 [31] A. W. Bushmaker, V. V. Deshpande, M. W. Bockrath, S. B. Cronin, *Nano Lett.* **2007**, *7*, 3618.  
 [32] V. Deshpande, S. Hsieh, A. Bushmaker, M. Bockrath, S. Cronin, *Phys. Rev. Lett.* **2009**, *102*, 105501.  
 [33] E. Pop, D. Mann, J. Cao, Q. Wang, K. Goodson, H. Dai, *Phys. Rev. Lett.* **2005**, *95*, 155505.  
 [34] M. R. Amer, A. Bushmaker, S. Cronin, *Nano Res.* **2012**, *1–9*, 172.

Received: November 16, 2014  
 Revised: February 7, 2015  
 Published online: